Supplemental material for "A power-based abrasion law for use in landscape evolution models"

DD Hansen[1], JP Brooks[1], LK Zoet[1], NT Stevens[1], L Smith[1], CEBate[2], BJ Jahnke[2]

[1]*Department of Geoscience, University of Wisconsin-Madison, 1215 W. Dayton St., Madison, Wi, 53715*

[2]*Department of Geological Engineering, University of Wisconsin-Madison, 1415 Engineering Dr., Madison, Wi, 53706*

Contains Supplemental Texts:

- S1 Direct Shear: experimental protocol
- S2 Ring shear: experimental protocol
- S3 Measuring abraded volume
- S4 Grain size distribution of rock gouge,
- S5 Surface Fracture Energy
- S6 Estimating E_a and associated uncertainty with a Monte Carlo Markov Chain approach

S1. Direct Shear: experimental protocol

We conducted glacial abrasion experiments using an ELE International direct shear device with a custom sample chamber made of low-thermal conductivity fiberglass (Fig. S1), following the methodology of Hansen and Zoet (2019). Beds of two different lithologies (oolitic Indiana limestone and marble, sized 10 x 10 cm) were slid beneath debris-laden temperate ice over a range of bed-normal forces. When sourcing granitoid clasts from till, carbonate clasts were identified through an acid reaction test and visual inspection and subsequently discarded. Clasts diameters were approximately equal or less than one-tenth the width of the sample chamber and less than half its height to avoid boundary effects (Head, 1989). Further details concerning the direct shear device and the experimental protocol can be found in Hansen and Zoet (2019). Table 1 lists the boundary conditions implemented in these experiments. Values for shear stress τ_r (or shear force, $F_s = \tau_r A$) reported herein represent mean values calculated from the measured drag over the full slip displacement. Normal stresses (σ_n) for the direct shear are applied by weights hung from a lever arm and therefore constant. For each apparatus, we measured a background drag for clean ice, and then subtracted it from the measured shear stress to isolate rock friction ($0.1216\sigma_n$ for limestone and $0.0372\sigma_n$ for marble).

S2 Ring shear: experimental protocol

We also conducted two abrasion experiments in a cryogenic, temperature-controlled ring shear device, hereafter denoted RS1 and RS2 (Fig. S2). This apparatus better approximates subglacial drainage conditions compared to the direct shear and effectively allows unlimited displacement. (For a detailed description of this device refer to Hansen and Zoet, 2022.) We slid rings of debris-laden temperate ice over marble beds at prescribed normal stresses, basal melt rates, and slip speeds (see Table 1 for boundary conditions). For these two experiments, we closely followed the experimental protocol of Thompson et al. (2020) with the following minor deviations: i) we sequentially built our ice ring in 5–10-cm-thick layers of snow and deionized water instead of 1–2 cm-thick layers, and ii) we estimated vertical drawdown solely using the linear variable displacement transducer (LVDT) without tracking beads. Between RS1 and RS2, there were two differences in methodology. First, in RS2, we froze clasts to the bed in a ~3-mm-

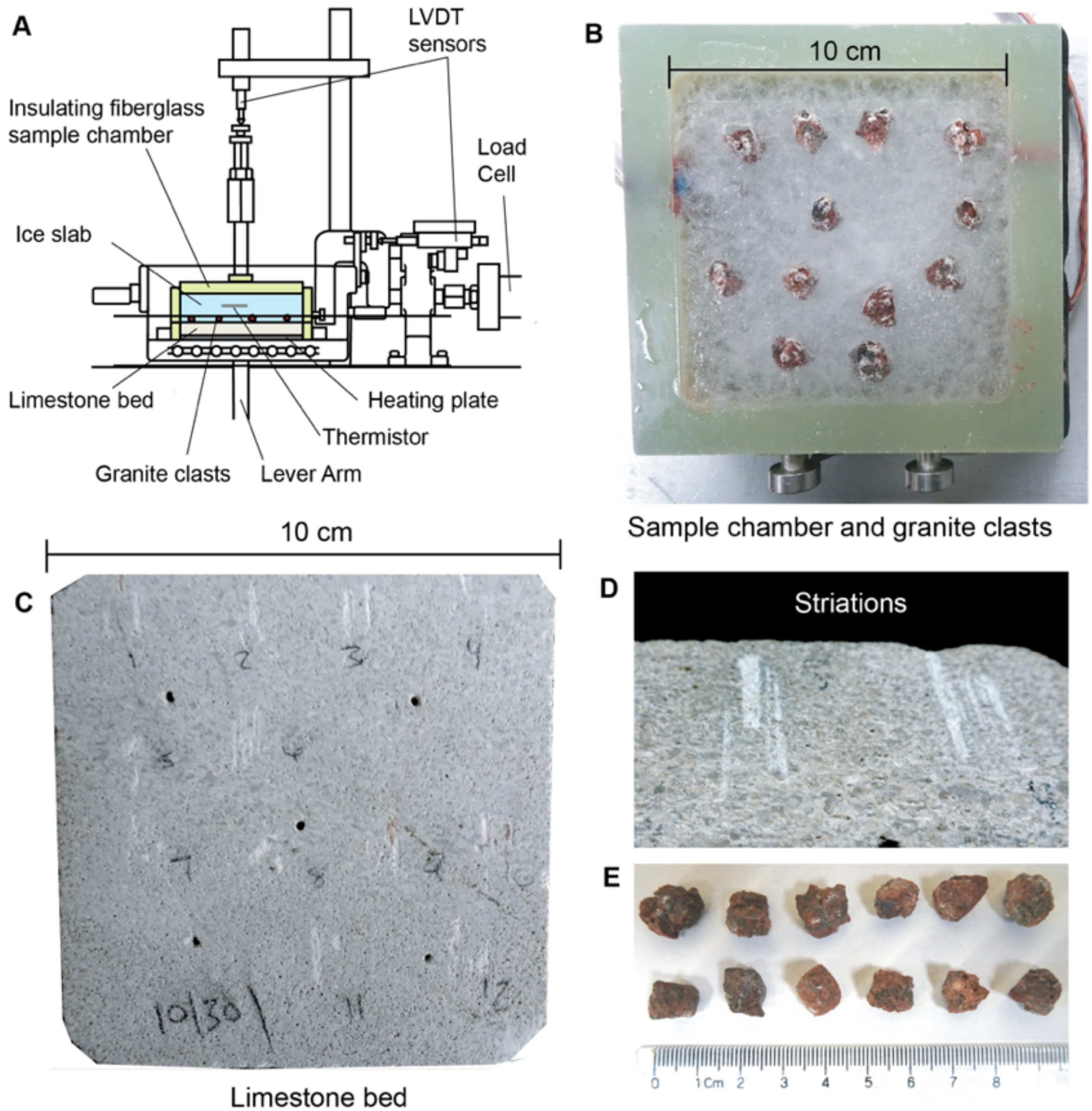

Figure S1. (a) A schematic of the modified direct shear device, (b) debris-laden ice within the insulating sample chamber, (c) a typical limestone bed at the conclusion of an experiment (note that multiple striations are common for a single abrading rock), (d) striations, and (e) 12 representative granite clasts used in our experiments. Figure copied from Hansen and Zoet (2019).

thick film of ice before constructing the ice ring, which may have caused more clasts to be in contact with the bed than in RS1. Second, we recorded temperature in RS2 with four glass bead thermistors installed in the base, 8 in the outer sample chamber walls, and a GEC temperature probe mounted in the glycol/water bath at the level of the ice bed interface; whereas RS1 only had the GEC probe. Since we are not concerned with the relationship between specific controls such as melt rate or debris concentration and abrasion in this study, these differences do not impact on our interpretation.

In poorly drained environments, debris-bed contact forces are primarily controlled by the pressure gradients in thin water films surrounding entrained clasts and the real area of contact between the clasts and the bed, with negligible contribution from ice pressure (Thompson et al., 2020). In similar ring shear experiments, Thompson et al. (2020) reported that ice pressure exerted no influence on contact forces, even though the chamber was connected to atmospheric pressure. They did, however, observe a nonlinear dependence on basal melt rate. Accordingly, we increased the contact force in RS2 relative to RS1 by raising the temperature in the circulating glycol-water bath. This induced a higher melt rate at the interface, and a LVDT recorded drawdown as the sample contracted. For both experiments, the slip speed of basal ice equaled 37.5 m/yr at a radial position that divided the bed into two equal areas (r_{cl} = 0.22 m). Similar to Thompson et al., 2020, the grain size distribution was comprised of three size classes with the number of clasts in each corresponding to a fractal dimension of 2.9 (Hooke and Iverson, 1995). This resulted in an areal debris concentration at the bed of 10% and ~4% volumetric concentration assuming clasts were similarly spaced across the bed (Thompson et al., 2020). In total, we used 212 small clasts (5-12 mm diameter), 72 medium clasts (12-20 mm), 25

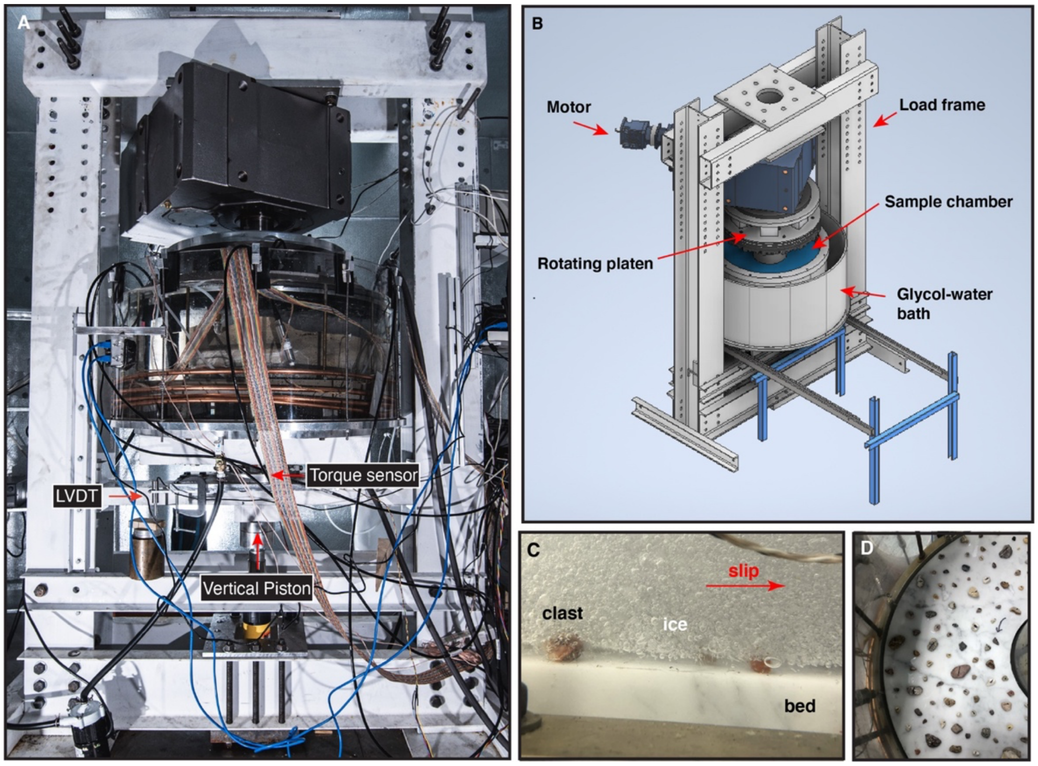

Figure S2. A) Photo of the cryogenic ring shear device. B) design schematic (modified from Dodge et al, 2022). C) clast entrained in ice slipping on a marble bed at the outer sample chamber wall. D) Clasts arrayed on marble bed prior to building the ice ring. (Photo credit: Ethan Parrish)

76

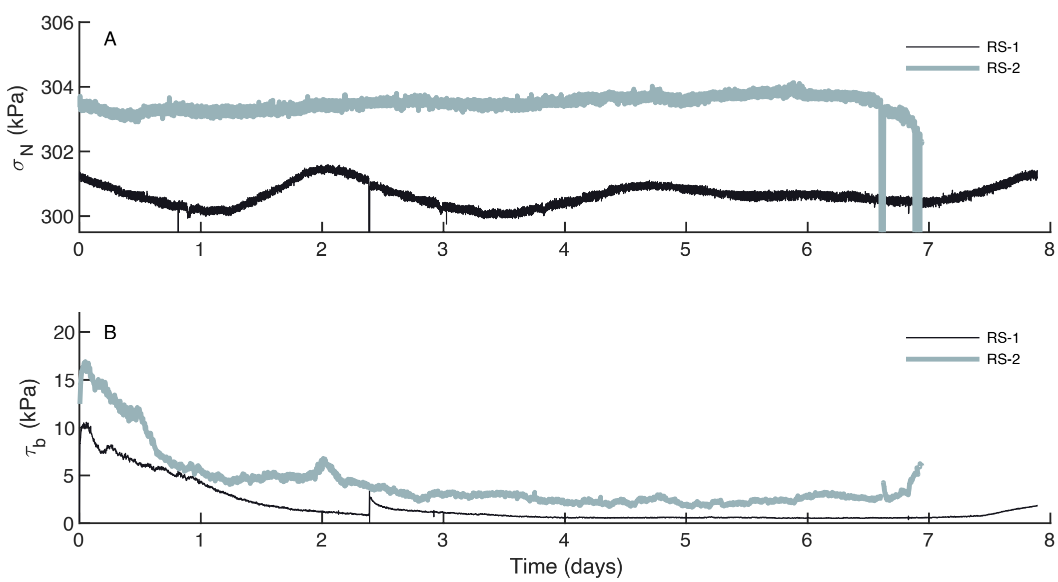

Figure S3. Experimental time series for the two ring shear experiments, RS1 and RS2, showing a) the normal stress applied by a hydraulic ram, and b) the basal shear stress recorded during slip, τ_r. The x-axis denotes time since slip was initialized by rotating the ice ring.

large clasts (20-28 mm). All clasts were igneous or metamorphic and sourced from the same Horicon till.

S3. Measuring abraded volume

We scanned striations with a Nanovea JR 25 white light profilometer to create digital elevation models (DEM) of the abraded surface (Fig. 1). Abraded volume for each surface DEM was calculated using proprietary functions in Nanovea's analytic software, Professional 3D 7.4. To process a scanned surface, we applied the following workflow: First we corrected for any systematic background tilt introduced by unevenness of the scanning platform with a leveling function, which fit a plane to the surface using least squares regression and then subtracted it from the DEM point by point. Next, we identified and replaced spurious points with values interpolated from neighboring valid points. Volume and projected area for each striation were then calculated by manually defining a contour around the boundaries of a striation, fitting a least

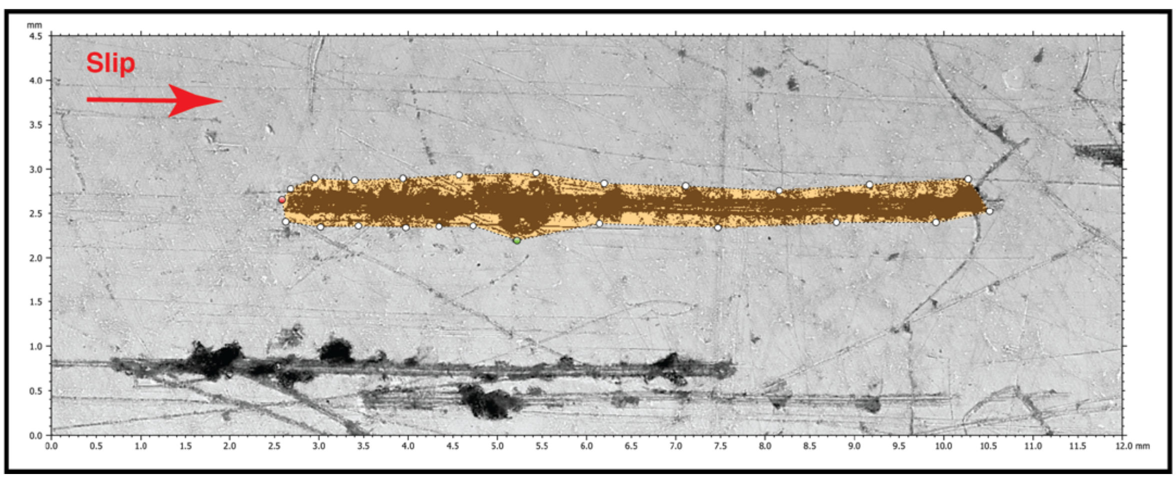

Figure S4. Striations produced in a marble-bed direct shear experiment that illustrate our method for calculating abraded volume. A contour is manually defined around the striation (dotted outline) and a plane is fit to the surrounding surface using ordinary least squares regression. The dark brown shaded region in this contour represents the region where surface elevation lies below this plane (a "hole") and the light orange shading represents the region where surface lies above ("a peak"). Abraded volume is then the volume of the void defined by the projected area of the holes, the elevation of this plane and the underlying surface.

squares plane to points outside of the user-defined contour, and then subtracting the difference between the surface defined by the contour and this plane (Fig. S4).

The time required to scan the marble ring shear bed at the highest resolution is prohibitive (~1300 hours per experiment), so we scanned the entirety of the marble bed at a lower resolution (20 μm X 150 μm) to mitigate the time cost. Pixel dimensions, however, increase at lower resolutions, smoothing roughness elements on the surface and producing more diffuse striation boundaries—factors which both affect the final volume calculation. To correct for this degradation, we estimated the relationship between pixel dimension and abraded volume for a set of nine striations. Individual features were scanned repeatedly at varying y-step sizes (10–150 μm) with a constant x-step of 20 μm. We calculated abraded volume for each set of striations using the method outlined above and normalized each set of volumes by the set value for y-step = 10 μm. An ordinary least squares solution suggests estimated striation volume decreases with y-step resolution at a rate of ~ -0.085% per μm increase in y-step size (Fig. S5). Therefore, we adjusted our measured volumes by +11.01% in line with a resolution of 20 μm X 20 μm, which was the resolution for most of the direct shear marble bed scans.

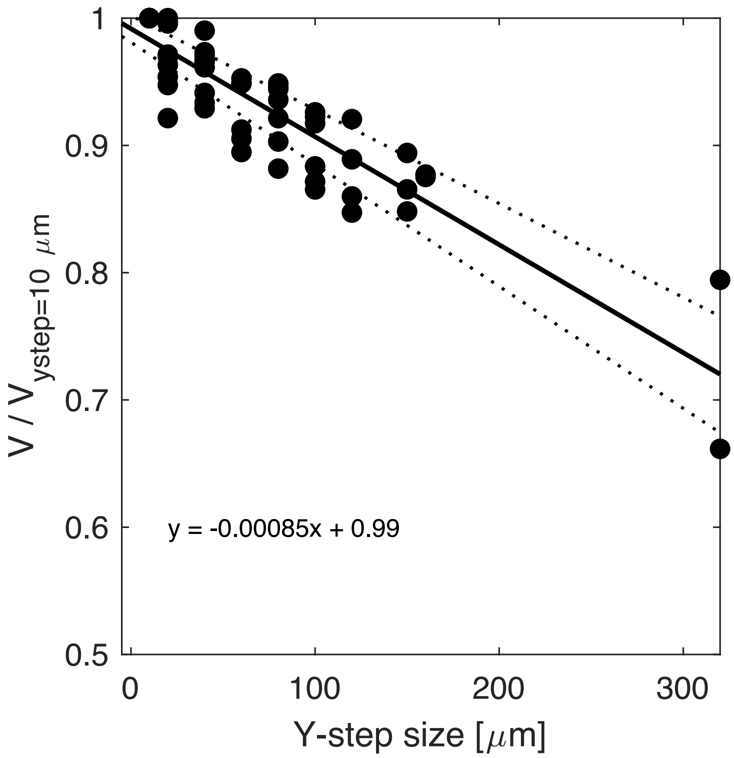

Figure S5. Abraded volume, V, normalized by V at y-step = 10 μm, decreases with increasing y-step resolution. Solid black line represents the ordinary least squares regression with associated standard error for the slope 5.5 x 10^{-5} μm^{-1} and $r^2 = 0.82$. Dashed lines represent 95% confidence intervals for the fit.

S4. Grain size distribution of rock gouge

Surface area created through abrasion is proportional to the grain size distribution of the gouge particles created during shear (Eq. 5). In our experiments, the particulate produced in a single experiment was minuscule and typically below the threshold mass needed for standard grain size analysis, so we conducted a separate set of tests in the direct shear to produce this material (~0.2 g per sample). Clasts (similar to those used in the main experiments) were encased in slabs of epoxy and slid over beds of both lithologies under a range of vertical stresses. Shear resistance in these runs arose solely from rock-rock on friction as no other portion of the slab contacted the bed. Following each experiment, we dusted the abraded slab to collect the particulate on its surface and repeated this process until we obtained the required mass. Between

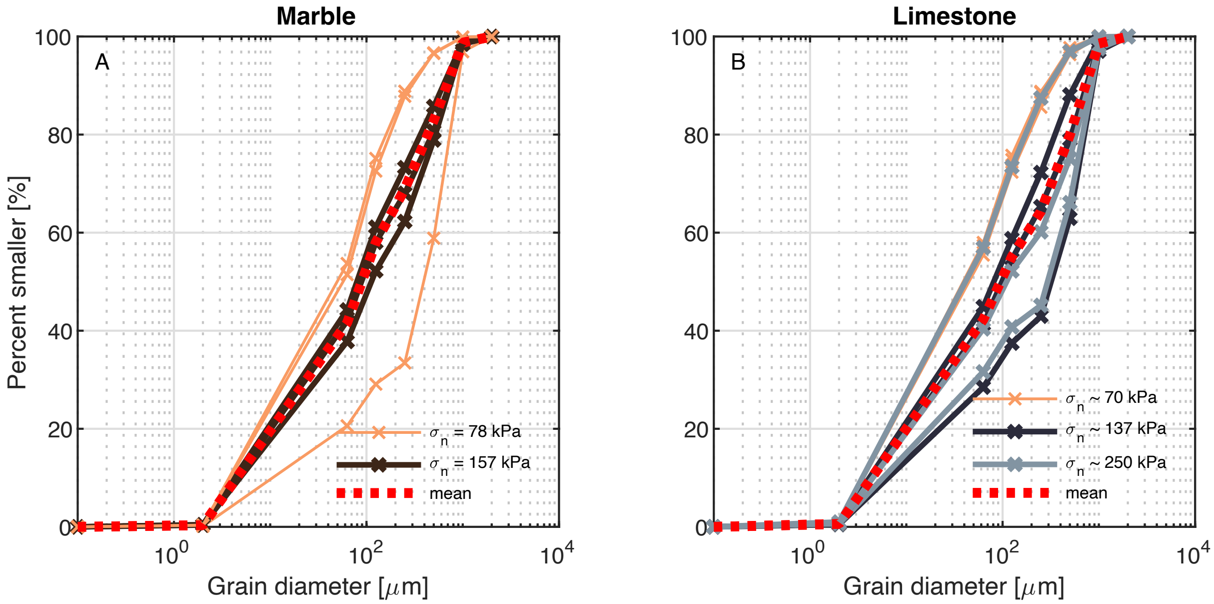

Figure S6. Grain size distribution of the gouge particles produced in epoxy/clast abrasion runs for the marble (a) and limestone (b) beds under different normal loads, F_n. Red dotted curves in each plot show the mean GSDs.

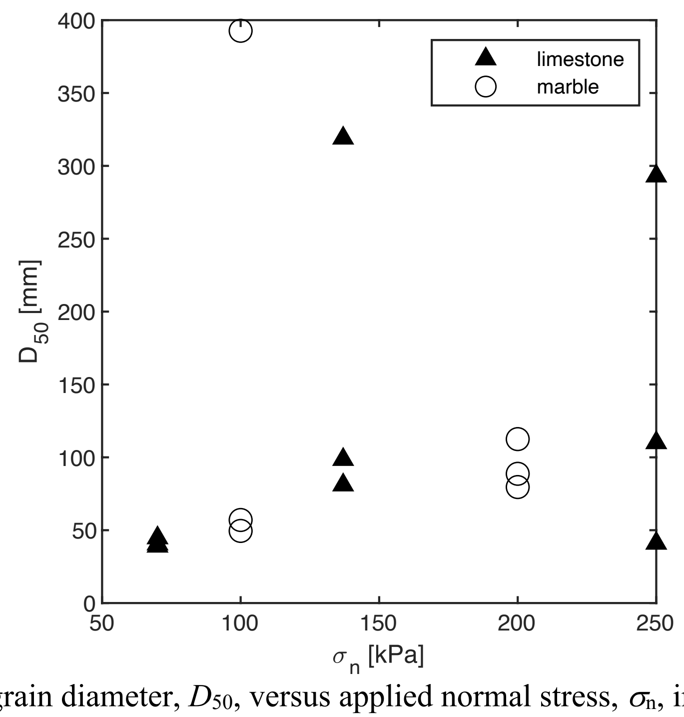

Figure S7. Median grain diameter, D_{50}, versus applied normal stress, σ_n, in the epoxy/clast direct shear runs for the marble (white circles) and limestone (black triangles) beds.

each run, we rotated the epoxy slabs or sanded the bed to prevent clasts from repeatedly abrading the same striation. Grain size distribution of the gouge was analyzed via laser diffraction in a Malvern Mastersizer 2000E at the University of Wisconsin-Milwaukee following standard procedure. Prior to the analysis, particles were dispersed in a 0.05% sodium phosphate solution for at least 24 hours to deflocculate aggregates and then sonicated for at least ten seconds. In total, we collected two gouge samples for the marble bed type (at σ_n = 78.4 and 156.8 kPa), and three samples for the limestone bed (at σ_n = 70, 137, 250 kPa). The grain size distribution for each sample was analyzed three times (Figure S6). We observed no clear trend between the imposed loads and the resultant grain size distribution (Fig. S6). Median grain diameter, D_{50}, ranged between 39–319 μm for the limestone gouge and 49.5–392.7 μm for the marble. Differences in D_{50} >100 μm measured for a single sample reflects the variable tendency of sand size particles to be mobilized during individual measurements. Therefore, for our purposes in Eq. 5, we opted to randomly sample distributions of each rock type when estimating E_a from 20,000 Monte Carlo Markov Chain simulations (S6). Mean distributions are denoted by dashed red lines in Fig. S6 with D_{50} = 89 μm and 95 μm for marble and limestone gouge respectively.

S5. Surface Fracture Energy

Surface fracture energy of polycrystalline rocks, γ, is the energy consumed during the creation of a new surface per unit area (Nakayama, 1965; Zhang and Ouchterlony, 2022). Irwin (1956) proposed a model for fracture that includes an energy release rate parameter, G, to represent the available energy for an increment of crack extension. When G reaches a critical value—i.e. $G_c = 2\gamma$—fracture occurs (Anderson, 2005). Likewise, Mode I fracture toughness

(K_c) describes a material's resistance to fracture propagation (ISRM, 1995) and relates similarly to G_c under mode I loading (Soboyejo, 2003):

$$G_c = \frac{K_c^2}{E'} \tag{S1}$$

where $E' = E/(1-v^2)$ for plane strain, E is Young's Modulus, and v is Poisson's ratio. It therefore follows that under Mode I loading:

$$\gamma = \frac{K_c^2(1-v^2)}{2E}. \tag{S2}$$

From this equivalency, we estimated γ for our limestone and marble beds for Eq. 3. We measured K_c with Cracked Chevron Notched Brazilian (CCNBD) disc tests and E and v with unconfined uniaxial compression tests (UCT). Both sets of experiments were conducted in a GCTS servo-controlled triaxial apparatus following suggested ISRM protocol (ISRM, 1979; ISRM, 1995).

CCNBD tests methods

We successfully conducted CCNBD tests on four limestone and seven marble samples. Fowell (1995) defined K_c as

$$K_c = \frac{F_{max}}{B \cdot \sqrt{r}} \, Y_m^* , \tag{S3}$$

where B and r are the thickness and radius of the notched disc respectively, and F_{max} is the normal force applied to the disc at the moment of failure. Y_m^* is the minimum critical stress intensity factor, which for valid disc geometries is

$$Y_m^* = u \cdot e^{v \cdot \alpha_1}, \tag{S4}$$

where u and v are geometrical constants listed in ISRM (1995), $\alpha_1 = a_1/R$, and a_1 is one half the outer notch length. Cylindrical discs were cut from longer cores using a high-precision saw and notched with a Dremel tool (Fig. S7A). Average sample dimensions were $2r \sim 37.9$ mm, $B \sim 12.7$ mm, with an outer notch length $2a_1 \sim 26.2$ mm and inner notch length of $\sim 2a_0 \sim 10.4$ mm. We identified F_{max} by plotting applied load versus lateral displacement and identifying the point where an initial stress drop coincided with rapid lateral expansion (Fig. S7 C–D). Parameters u and v were interpolated from the table of values provided in ISRM (1995) to correspond to our specific disc dimensions. Table S1 presents these results.

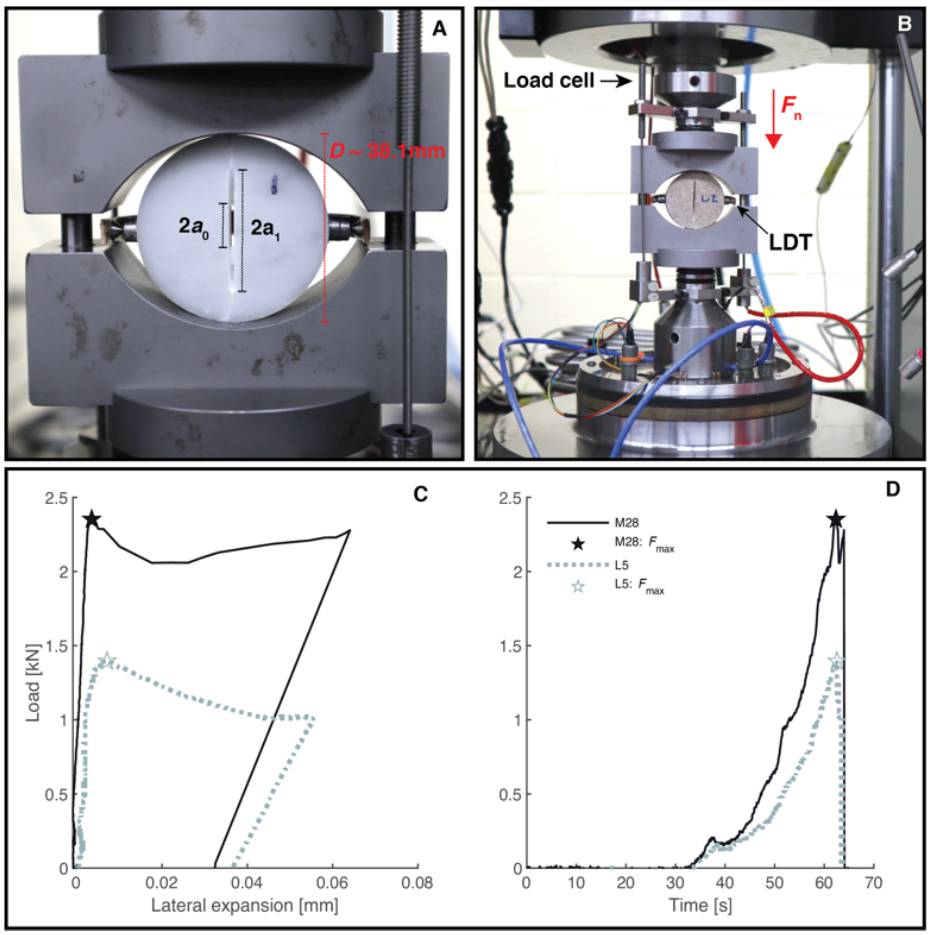

Figure S7. A) Notched disc for CCNBD seated in the loading frame. B) a vertical force, F_n, is applied to the sample, while an LDT records horizontal displacement and an LVDT measures vertical displacement. C) Applied load versus lateral expansion for a representative limestone run (grey dashed line) and a marble run (solid black line). The stars denote the point of failure, F_{max}, identified as the point where a sudden drop in load occurs simultaneously with rapid horizontal expansion. D) A timeseries of the applied load for the same two runs. Stars represent the same F_{max} in S7C.

Table S1. Summary of CCNBD tests parameters and results[†]

ID	Rock	$2a_0$ [mm]	$2a_1$ [mm]	B [mm]	$2r$ [mm]	F_{max} [kN]	K_c [MPa m$^{0.5}$]
L3	LS	11.72 ± 0.051	26.77 ± 0.051	12.68 ±0.013	37.90 ± 0.064	1.42	0.788
L4	LS	11.74 ± 0.013	26.66 ± 0.88	12.84 ± 0.089	37.89 ± 0.013	1.35	0.735
L5	LS	11.56 ± 0.076	26.02 ± 0.13	12.65 ± 0.051	37.91 ± 0.10	1.395	0.747
L6	LS	7.45 ± 0.076	25.54 ± 0.99	13.03 ± 0.051	37.85 ± 0.013	1.174	0.574
M1_1	M	10.6 ± 0.3	26 ± 0.0	12.5 ± 0.0	38.0 ± 0.0	2.12	1.12
M1_3	M	10.23 ± 0.1	26 ± 0.0	12.5 ± 0.0	38. 0 ± 0.0	1.797	1.47
M2_1	M	9.13 ± 0.07	26.19 ± 0.65	12.53 ±0.04	37.97 ± 0.3	2.1	1.08
M2_3	M	10.40 ± 0.32	26.48 ± 0.58	12.95 ± 0.02	37.91 ± 0.04	2.8	0.95
M2_6	M	10.81 ± 0.15	26.59 ± 0.32	13.38 ± 0.08	37.89 ± 0.00	2.103	1.28
M2_7	M	10.31 ± 0.34	26.04 ± 0.16	12.12 ± 0.04	37.89 ± 0.03	1.715	1.17
M2_8	M	10.58 ± 0.22	26.08 ± 0.9	12.44 ± 0.18	37.88 ± 0.02	2.352	0.95

[†]Sample ID; Rock type (M=marble and LS=limestone); Outer notch length, $2a_0$; inner notch length $2a_1$; sample thickess, B; sample diameter, $2R$; load at moment of fracture, F_{max}; minimum critical stress intensity factor, Y_m^*; Fracture toughness, K_c. For parameters $2a_0$, $2a_1$, B; and $2R$, "±" denotes the range of 2–3 measurements. -

Estimating Young's Modulus and Poisson's ratio

We conducted unconfined uniaxial compression tests to determine the elastic parameters of the marble and limestone beds (Young's modulus, E, and Poisson's ratio, v). We tested three cylindrical samples for each bed type (average length: L ~ 50.60 mm, and average outer diameter: D ~ 25.55 mm; see Table S2), which were cored from larger blocks and ground to size on a precision surface grinder (Fig. S8A). Prior to loading, samples were jacketed in a polyolefin heat shrink for platen stability and fixed between two steel loading platens with a 25.4 mm diameter. Two diametrically opposed LVDTs mounted parallel to the sample's axis recorded longitudinal compression, while two lateral displacement transducers (LDTs) mounted at 90˚offsets recorded horizonal expansion as the rock deformed (Figure S8 B). At the start of each test, a constant seating stress of 1 MPa was applied to the sample over a 60 s interval. Axial load was then increased at a constant rate of 40 MPa/min, while we monitored for signs of sample failure. Once the sample begin to yield plastically, axial load was ramped down to 1 MPa at a rate of -40 MPa/min (except for sample Marb1, which was ramped down over a ten-minute interval instead). Two limestone samples ultimately failed under load whereas the rest remained intact.

For a linear elastic rock under uniaxial compression, $E = \sigma_n/\varepsilon_l$, where σ_n is the applied normal stress, $\varepsilon_l = \Delta L/L$ is the longitudinal strain, and ΔL is the change in sample length. By convention, σ_n and ε_l are negative in compression. We take the average of the two LVDT records for ΔL and subtract the deformation of the loading platens using a pre-determined fit. Poisson's ratio is $v = -\varepsilon_t/\varepsilon_l$, where $\varepsilon_t = \Delta D//D$ is the transverse strain, and ΔD is the change in sample diameter (average of two LDT records). We estimate E and v by computing the ordinary least squares solution over an interval where the relationships are approximately linear (assuming no plastic deformation) (Figure S8 C–F). For marble, the mean values were $E_m = 54.13 \pm 6.050$ and $v_m = 0.3342 \pm 0.0523$, and for limestone $E_{ls} = 23.02 \pm 10.02$ and $v_{ls} = 0.2196 \pm 0.1189$ (where "±" denotes the range of three samples). Table S2 presents these results.

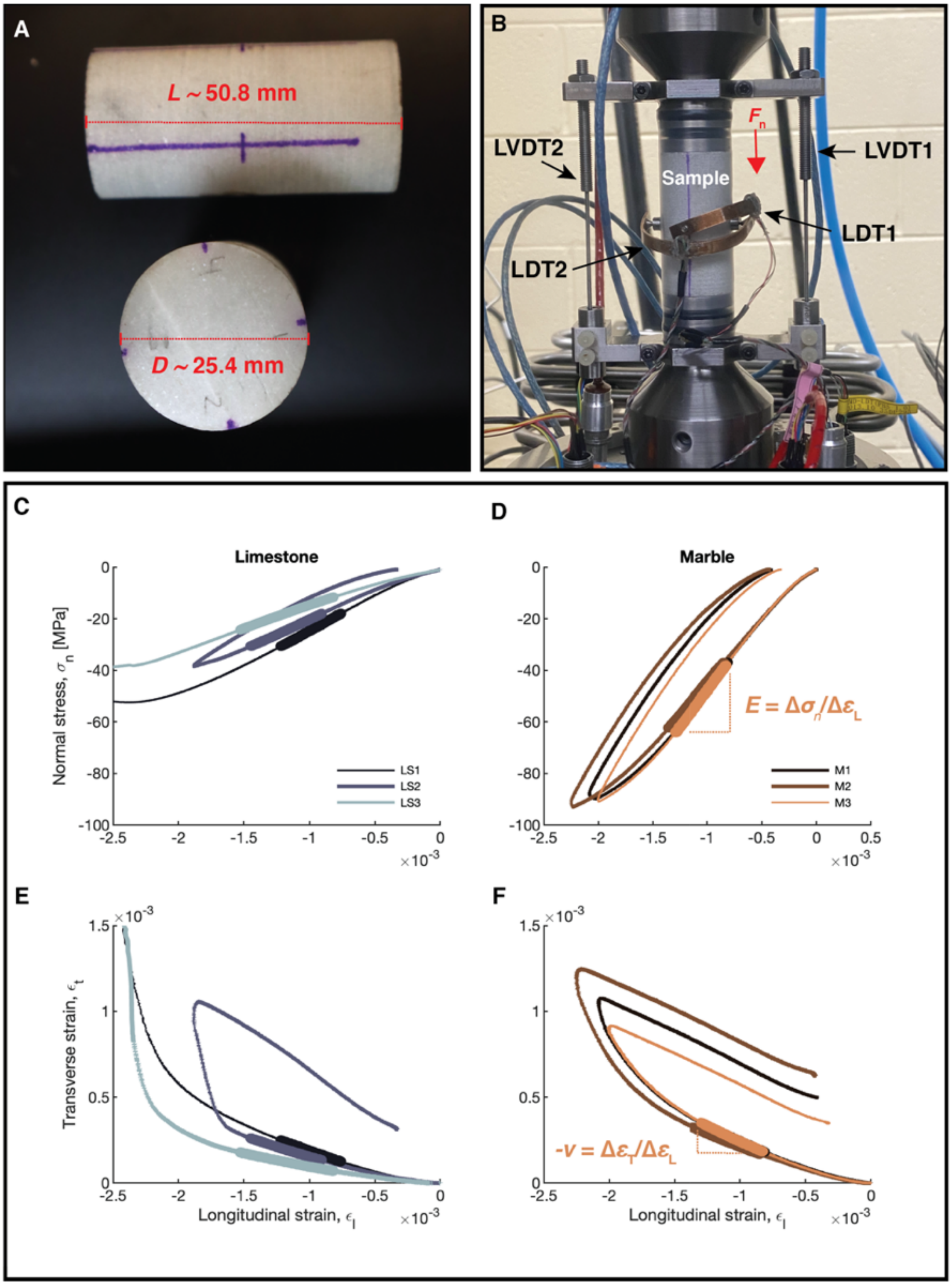

Figure S8. A) sample dimensions, B) the loading apparatus applied a vertical load, F_n, to the sample while LVDTs and LDTs measure vertical and horizontal displacement, respectively. C–D) Longitudinal strain, ε_l, versus applied normal stress, σ_n. E–F) Longitudinal strain versus transverse strain. Thicker line segments show the interval over which E and ν were estimated with an ordinary least-squares solution.

Table S2. Summary of unconfined uniaxial compression tests and results.

	L [mm]	D [mm]	*E* [GPa]	*v*
LS1	50.44 ± 0.05	25.37 ± 0.24	27.82 ± 0.02115	0.2705 ± 0.0003043
LS2	50.53 ± 0.05	25.55 ± 0.01	23.44 ± 0.01465	0.2366 ± 0.0002521
LS3	50.61 ± 0.02	25.49 ± 0.14	17.80 ± 0.01033	0.1516 ± 0.0001862
Marb1	50.60 ± 0.05	25.60 ± 0.16	55.42 ± 0.02213	0.3424 ± 0.0002639
Marb2	50.81 ± 0.03	25.71 ± 0.02	50.46 ± 0.02509	0.3039 ± 0.0002449
Marb3	50.65 ± 0.03	25.58 ± 0.15	56.51 ± 0.02931	0.3562 ± 0.0002739

†Sample ID; Rock type (Marb=marble and LS=limestone); Sample length, *L*; Sample diameter, *D*; Young's modulus, *E*; and Poisson's ratio, *v* . For parameters *L* and *D*, "±" denotes the range of four and three measurements, respectively. Otherwise "±" states the standard error associated with the ordinary least squares solution.

S6. Estimating E_a and associated uncertainty with a Monte Carlo Markov Chain approach

Calculations of E_a using Eq. 3 Eq. 3–5 and S1–S4 incorporated numerous experimental measurements with small sample sizes (generally $n \leq 5$); however, each sample has known observational uncertainties. To propagate experimental uncertainties through this system of equations, we used a Monte Carlo Markov Chain (MCMC) approach with 20,000 simulations for each experimental geometry and lithology, randomly drawing perturbed values from prior distributions of individual measurements (Table S3). We described observed data values using uniform distributions for length-scale measurements (L, D, $2a_0$ $2a_1$, $2r$, and B), scaling distributions by relevant measurement precision, along with roughness prefactor R (Eq. 5), which ranges from 3–5 (Fulton and Rathbun, 2011). For parameter estimates E and v obtained from linear regression of experimental data, we used Gaussian prior distributions centered on the regression slope values (F_n vs. ΔL and ΔD vs. ΔL) and scaled by the modeled slope variance. The slopes were combined with estimates of D, L, and A to obtain E and v. Perturbed grain-size values were drawn from empirical distributions in Fig. S6, and all prior distributions are documented in the data repository with repeat measurements. Rather than averaging repeat measurements, we drew samples from measurement prior distributions. We also randomly selected a single K_c, E, and v from the set of possible values computed for the sample set (i.e. marble versus limestone). This mitigated biases in the posterior distributions of E_a that could arise from small sample sizes. Posterior distributions of E_a are all skewed rightward (Fig. S9), so we use the median and median absolute deviation (MAD) to calculate reported values in the main text.

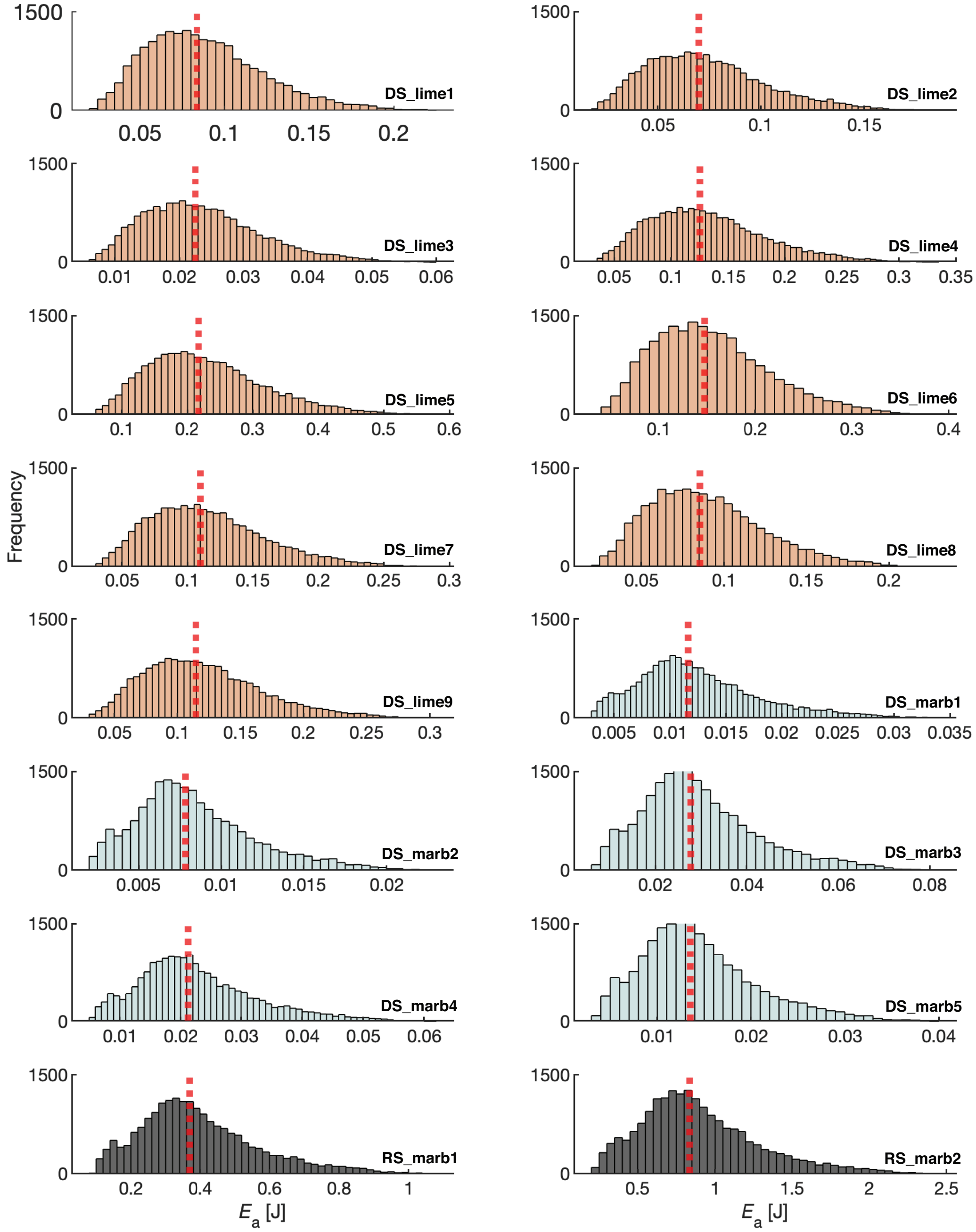

Figure S9. Frequency of estimated abrasion energy, E_a, computed with 20,000 MCMC runs for the limestone-bed direct shear experiments (copper), marble-bed direct shear experiments (grey), and marble-bed ring shear experiments (black). Red dashed lines denote the median of the set.

DATA AVAILABILITY

Data for this manuscript is permanently archived at https://minds.wisconsin.edu/handle/1793/83718.

SUPPLEMENTAL REFERENCES

Anderson, T. L., 2005, Fracture mechanics: fundamentals and applications, 3rd edn. Taylor and Francis Group, London

Bieniawski, Z. T. and Bernede, M. J., 1979, Suggested methods for determining the uniaxial compressive strength and deformability of rock materials: Part 1. Suggested method for determining deformability of rock materials in uniaxial compression. International Journal of Rock Mechanics and Mining Sciences, v. 16, p. 138-140.

Fowell, R.J., 1995, ISRM commission on testing methods. Suggested method for determining mode I fracture toughness using cracked chevron notched Brazilian disc (CCNBD) specimens. International Journal of Rock Mechanics and Mining Sciences, v. 32, p.57-64.

Fulton, P.M. and Rathbun, A.P., 2011, Experimental constraints on energy partitioning during stick–slip and stable sliding within analog fault gouge: Earth and Planetary Science Letters, v. 308, p. 185-192, doi:10.1016/j.epsl.2011.05.051.

Hansen, D.D. and Zoet, L.K., 2019, Experimental constraints on subglacial rock friction: Annals of Glaciology, v. 60, p. 37-48, doi:10.1017/aog.2019.47

Hansen, D.D. and Zoet, L.K., 2022, Characterizing sediment flux of deforming glacier beds: Journal of Geophysical Research: Earth Surface, v. 127(4), p. e2021JF006544, doi: 10.1029/2021JF006544.

Head, K. H., 1989, Soil technicians' handbook (No. 624.151 H4). Pentech Press.

Irwin, G.R., 1956, Onset of fast crack propagation in high strength steel and aluminum alloys. Sagamore Research Conference Proceedings. p. 289–305.

Nakayama, J., 1965. Direct measurement of fracture energies of brittle heterogeneous materials. *Journal of the American Ceramic Society*, *48*(11), pp.583-587.

Thompson, A.C., Iverson, N.R. and Zoet, L.K., 2020, Controls on subglacial rock friction: Experiments with debris in temperate ice: Journal of Geophysical Research: Earth Surface, v. 125, p. e2020JF005718, doi:10.1029/2020JF005718.

Zhang, Z.X. and Ouchterlony, F., 2021, Energy requirement for rock breakage in laboratory experiments and engineering operations: A review. Rock Mechanics and Rock Engineering, p.1-39.